NJC

Accepted Manuscript

This is an *Accepted Manuscript*, which has been through the Royal Society of Chemistry peer review process and has been accepted for publication.

Accepted Manuscripts are published online shortly after acceptance, before technical editing, formatting and proof reading. Using this free service, authors can make their results available to the community, in citable form, before we publish the edited article. We will replace this *Accepted Manuscript* with the edited and formatted *Advance Article* as soon as it is available.

You can find more information about *Accepted Manuscripts* in the Information for Authors.

Please note that technical editing may introduce minor changes to the text and/or graphics, which may alter content. The journal's standard Terms & Conditions and the Ethical guidelines still apply. In no event shall the Royal Society of Chemistry be held responsible for any errors or omissions in this *Accepted Manuscript* or any consequences arising from the use of any information it contains.

ROYAL SOCIETY OF CHEMISTRY

www.rsc.org/njc

Theoretical investigation on the photophysical properties of a series of iridium(III) complexes with different substituted 2,5-diphenyl-1,3,4-oxadiazole†

Xiaohong Shang, *[a] Yanan Li, [a] Qing Zhan [b] and Gang Zhang [c]

[a]*College of Chemistry and Life Science, Changchun University of Technology, Changchun 130012, P.R. China. E-mail: shangxiaohong@ccut.edu.cn*

[b]*Jilin Provincial Institute of Education, Changchun 130022, P.R. China*

[c]*Institute of Theoretical Chemistry, Jilin University, Changchun 130023, P.R. China*

† Electronic supplementary information (ESI) available.

A quantum chemical investigation are made on several homoleptic iridium complexes [$(C^{\wedge}N)_2$Ir(pic)] with the 2,5-Diaryl-1,3,4-oxadia-zoles moiety in $C^{\wedge}N$ ligands, where pic represents picolinate anciliary ligand, from the structural and electronic properties and some charge-transport parameters viewpoints. It is intriguing to note that complex **2** exhibits its blue phosphorescent emission with maxima at 485 nm. Furthermore, to obtain the mechanism of high phosphorescence yield in **2**, we approximately estimate the radiative rate constant k_r , the contribution of ^{3}MLCT in the T_1 state, S_1-T_1 energy gap $\Delta E_{S_1\text{-}T_1}$, and the transition dipole moment in the $S_0 \rightarrow S_1$ transition μ_{S_1} for **2**. The comparison between the calculated results of the four complexes shows that the designed complex **2** may possess higher photoluminescent quantum efficiency than the others, which is the potential candidate as an efficient blue emitting material.

Introduction

Phosphorescent materials based on heavy transition metal complexes, particularly the iridium complex, have attracted much attention due to their potential application as highly efficient electron luminescent emitters in organic light emitting diodes (OLED).[1-3] The phosphors can utilize both singlet and triplet excitons, resulting in a theoretical level of unity for the internal quantum efficiency in phosphorescent OLEDs.[4,5] The short radiative lifetimes of Ir(III) emitters could reduce the probabilities of triplet triplet annihilation (at high current densities), which may lead to a significant decrease in photoluminescence quantum efficiencies. In addition to the application in optoelectronic devices, Ir(III) complexes have also exhibited promising applications as chemosensors and bioimaging materials due to their excellent photophysical properties.[6,7]

Up to now, many classes of neutral Ir(III) complexes with tunable emission colors have been exploited. To achieve Ir(III) complexes in which light emission predominates over nonradiative decay, choosing congruent ancillary ligand or introducing a variety of donating or accepting groups on the ligands is a feasible approach to suppress the activation of metal-centered (MC) d-d states and enhance the blue phosphorescence.[8.9]

According to the recent reports, materials with 2,5-Diaryl-1,3,4-oxadia-zoles (OXDs) are widely used as electron transporting and hole blocking materials in OLEDs because of their moderate electron affinity, high photoluminescence quantum yield, and good thermal and chemical stabilities.[10,11] In addition, the OXDs have only rarely been used as C^N ligands in cyclometalation reactions. Thus, Bryce et al. reported a class of iridium complexes with the OXDs moiety in C^N ligands and pic represents picolinate anciliary ligand.[12] In this study, four molecules (**1**–**4**) with acetylacetone and picolinate anciliary ligands in Fig. 1 have been studied by using the density functional theory (DFT).

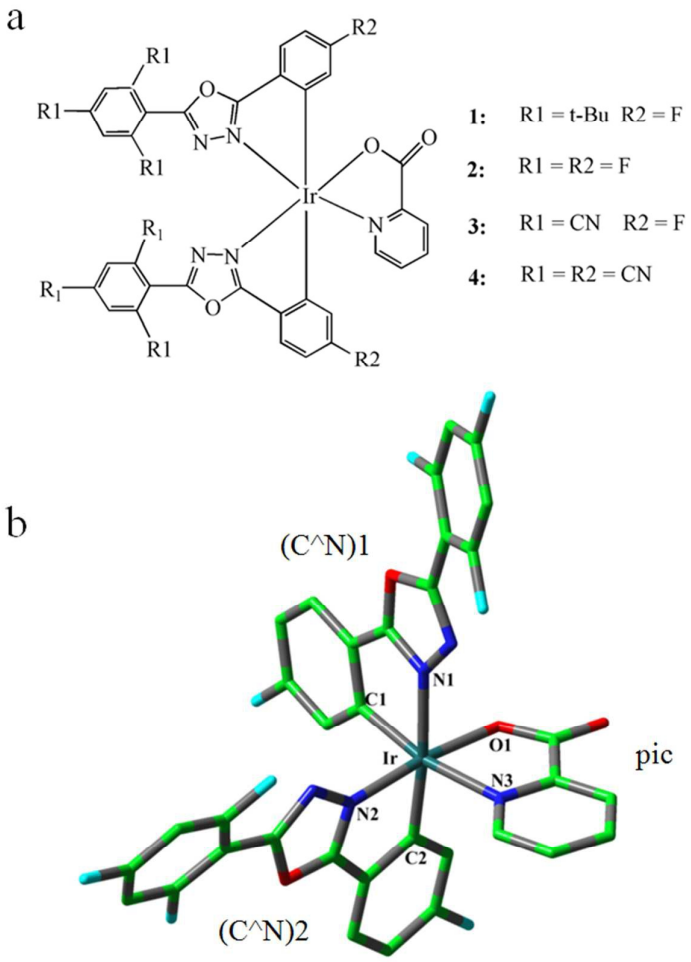

Fig. 1 (a) Sketch map of the structures of iridium(III) complexes **1**–**4;** (b) Representative optimized structure of **2** (H atoms omitted).

Furthermore, we also have investigated the relationship between the structures of the cyclometalated ligands and spectroscopic properties of these iridium(III) complexes. The computational results have been compared with the available experimental data. The electronic structures, charge injection, transport, spectral properties and photoluminescent quantum efficiencies are also discussed on the basis of these calculated results.

Computational details

The singlet ground state (S_0) and the first triplet excited state (T_1) for each complex were optimized by using the density functional theory (DFT) with hybrid-type

Perdew–Burke–Ernzerhof exchange correlation functional (PBE0),[13,14] which has been proven to be particularly efficient and accurate for the calculation of transition metal complexes and organic dyes.[15,16] Vibrational frequencies were calculated at the same theoretical level to confirm that each configuration was a minimum on the potential energy surface. To obtain the absorption and emission spectral properties, time dependent DFT (TD-DFT)[17-19] calculations associated with the polarized continuum model (PCM)[20-22] in dichloromethane (CH_2Cl_2) were performed on the basis of the optimized ground- and lowest triplet excited-state equilibrium geometries. Meanwhile, four different density functional (M06HF[23], M062X,[24] M052X,[25] and B3LYP[26]) were performed to calculate the emission spectra for **1**, aimed at finding the method that would allow for the reliable prediction of emission properties. The calculated results reveal that the M06HF functional gave more satisfactory emission properties for these Ir(III) complexes. In all calculations, a "double-ξ" quality basis set LANL2DZ[27] associated with the pseudopotential was employed on the iridium atom, in which a relativistic effective core potential (ECP) on Ir replaces the inner core electrons, leaving only the outer core [$(5s)^2$ $(5p^6)$] and the $(5d^6)$ as the valence electrons of Ir(III). The 6-31G(d,p) basis set[28] was used for non-metal atoms in the gradient optimizations. All calculations were done with the help of the Gaussian 09 program package[29] and GaussSum 2.5[30] was used for orbital and UV/Vis spectral analysis. The GaussView 5.0 user interface was used for structures and orbitals manipulations.[31]

Results and discussion

Molecular geometries in ground state S_0 and triplet state T_1

The schematic structures of these studied complexes are shown in Fig. 1 (a). The optimized structure of complex **2** in the ground state (S_0) at the PBE0 level is given in Fig. 1 (b), along with the numbering used in this study. Selected bond distances and angles between Ir metal and coordinating atoms of **1**–**4** in the ground and lowest triplet states (T_1) together with the available X-ray crystallography data[12] of complex

1 are shown in Table 1.

Table 1 Main optimized geometry parameters for complexes **1**–**4**, along with the experimental data

	1		**2**		**3**		**4**	
	S_0/ Exptl.[a]	T_1	S_0	T_1	S_0	T_1	S_0	T_0
bond length (Å)								
Ir-C1	2.030/2.033	2.023	2.030	1.992	2.031	2.027	2.033	2.026
Ir-C2	2.010/2.022	2.013	2.009	2.020	2.008	1.998	2.008	2.007
Ir-N1	2.143/2.098	2.157	2.148	2.111	2.146	2.147	2.143	2.151
Ir-N2	2.018/1.993	1.945	2.016	1.977	2.013	1.965	2.014	1.950
Ir-N3	2.133/2.108	2.159	2.131	2.164	2.132	2.145	2.131	2.147
Ir-O1	2.066/2.055	2.065	2.063	2.051	2.057	2.046	2.054	2.038
bond angle (°)								
C1-Ir-N3	170.0/172.1	170.3	170.4	170.5	170.0	169.8	169.6	169.7
C2-Ir-N1	173.5/173.6	173.9	173.3	174.4	172.8	173.5	173.1	172.2
O1-Ir-N2	173.5/175.2	173.8	173.0	173.7	173.2	173.7	173.1	174.3

[a] Ref. 12

In general, the calculated geometrical parameters are in close agreement with the measured values. The bond length deviation between the calculated and experimental ones is in the range 0.14–2.1 %. The largest discrepancies are for the Ir-N1 bond and C1-Ir-N3 bond angle, which deviate from the measured data by about 0.045 Å and 2.1° (see Table 1 for details), respectively. According to Table 1 and Fig. 1 (b), the calculated Ir-C2 and Ir-N2 bond lengths are significantly shorter than the corresponding Ir-C1 and Ir-N1 bond lengths at S_0 states; for example, the lengths of four Ir-C2 bonds for **1**–**4** are 2.010, 2.009, 2.008, and 2.008 Å, respectively, much shorter than those of the Ir-C1 bonds. This indicates that the interaction between the (C^N)2 ligand and the metal center is stronger than that between the (C^N)1 ligand

and the metal center.[32] Since the carboxylic in the pic ligand locates at the trans disposition of the pyrazole in the (C^N)2 ligand, and the indirect inductive effects via carboxylic make the electron delocalization transfer through the Ir ion and spread to the trans-oriented pyrazole ring, as a result, the bond length of Ir-N2 will be shortened. It is noted that the Ir-C, Ir-N and Ir-O bond lengths show negligible changes (within 0.011 Å) from **1** to **4**, indicating that the introduction of the fluorine, tertbutyl and cyano functional group in the phenyl moieties of C^N ligands causes a minor effect on the geometric structures.

To demonstrate the changes of geometry structures upon excitation, the geometry parameters of **1**–**4** in the lowest-lying triplet states were also calculated and listed in Table 1. For Ir-C1, Ir-N2 and Ir-O1 bond lengths, they are shortened significantly in T_1 states compared with those in S_0 states especially in **2**. Meanwhile, the Ir-N1 (the exception of **2**) and Ir-N3 bond lengths are elongated significantly especially for complex **1**. The only exceptional case are complexes **3** and **4**, in which Ir-C2 and Ir-N2 bonds are shortened, in T_1 state compared with S_0 state. The change for **3** and **4** indicates that the interaction between metal and one (C^N)2 ligand in T_1 state is strengthened, thus resulting in it possessing the most involvement in excited states.

Electronic structure

The detailed information of molecular orbital, including compositions, energies of metal and ligand orbitals are collected in Tables S1-S4 (ESI†) and Fig. 2.

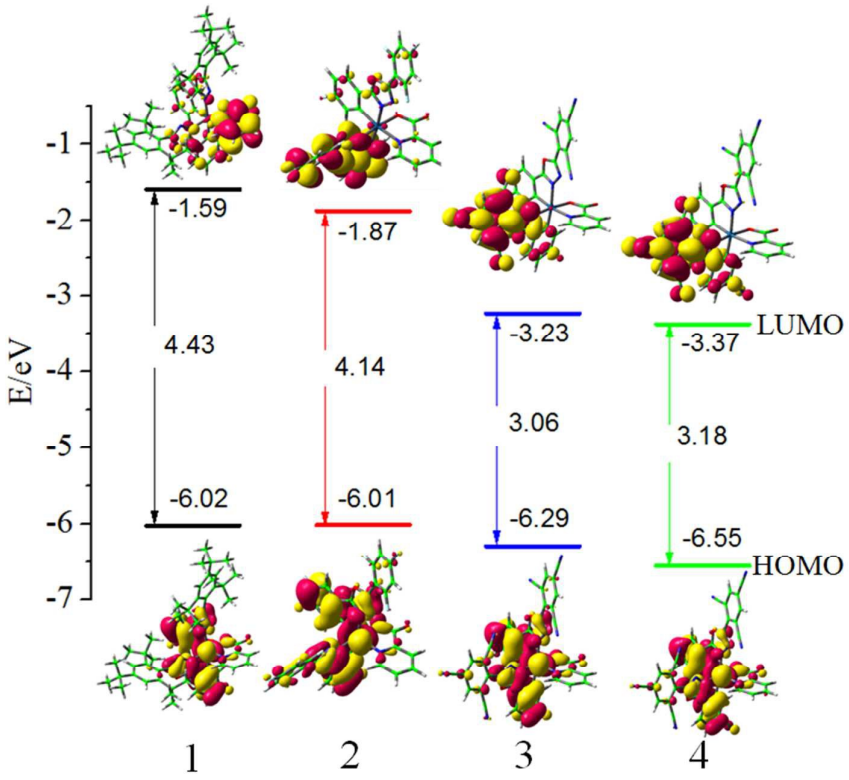

Fig. 2 Molecular orbital diagrams and HOMO and LUMO energies for complexes **1**–**4**.

Attaching different electron-withdrawing or electron-donating groups on C^N ligands does not cause obvious difference in HOMO distribution for **1**–**4**. For example, the HOMO mainly resides on the Ir 5d orbital with the composition of 42%, C^N ligands contribute 55%, and a small proportion (3%) for pic ligand in **1** (Table S1). The electron densities of the LUMO distribution are hardly influenced by different substitution on the phenyl moiety of C^N ligands in all complexes except that the LUMO distribution of **1** is mainly contributed by one of the pic ligand. This is consistent with the generally longer metal-(C^N)1 bond lengths in the ground states of these complexes (Table 1), which weakens the interaction between the metal and (C^N)1 ligand and consequently causes a smaller distribution on the (C^N)1 moiety (Tables S1–S4 (ESI†) and Fig. 2).

Fig. 2 shows that both the HOMO and LUMO energy levels are successively reduced from **1** to **4** with the variation of substitution in C^N ligands. In addition, the

LUMO is destabilized more markedly than that of the HOMO, leading to the decreasing order of HOMO-LUMO energy gaps: **1** (4.43 eV) > **2** (4.14 eV) > **4** (3.18 eV) > **3** (3.06 eV). It is noted that the cyano based in cyclometalated C^N ligands (**3** and **4**) not only dramatically affects the LUMO energy level, but also results in the stabilization of the HOMO energy level to a greater extent.

Electronic absorption spectra

TDDFT/PBE0 method with PCM in CH_2Cl_2 media has been used to study the nature and the energy of absorption spectra of these complexes on the basis of the optimized S_0 geometries. The simulated absorption curves for complexes **1**–**4** are depicted in Fig. 3.

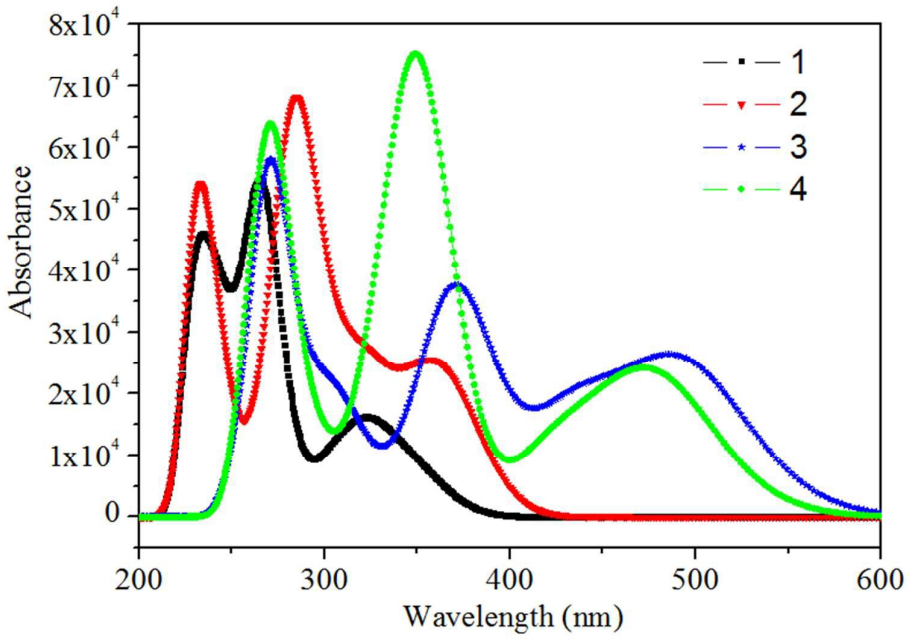

Fig. 3 Simulated absorption spectra in CH_2Cl_2 medium for **1**–**4**.

Meanwhile, the absorption energies, dominant configurations, and transition nature of the selected excited states with large oscillator strengths (*f*) are listed in Table 2 accompanying with the experimental result.

Table 2 Selected calculated wavelength λ(nm), oscillator strength *f*, major contribution, transition characters, and the available experimental wavelengths (nm) for complexes **1–4** (H Indicates HOMO, L Indicates LUMO)

	State	λ(nm)/E(eV)	*f*	Configuration	Assignment	Nature	Exptl.[a]
1	S_1	355/3.48	0.032	H→L(91%)	d(Ir)+π(C^N)→π*(pic)	MLCT/LLCT	
	S_{15}	287/4.31	0.154	H-3→L+1(77%)	π(C^N)→π*(C^N)	LLCT/ILCT	
	S_{18}	273/4.53	0.184	H-5→L (79%)	π(C^N)→π*(pic)	LLCT	256
	S_{32}	240/5.07	0.089	H→L+6(67%)	d(Ir)+π(C^N)→π*(C^N)	MLCT/LLCT/ILCT	
	T_1	434/2.85	0.000	H→L+1(47%)	d(Ir)+π(C^N)→π*(C^N)	MLCT/LLCT/ILCT	
2	S_1	370/3.34	0.192	H→L(90%)	d(Ir)+π(C^N)→π*(C^N)	MLCT/LLCT/ILCT	
	S_3	350/3.53	0.114	H→L+2(56%)	d(Ir)+π(C^N)→π*(pic)	MLCT/LLCT	
	S_6	323/3.83	0.132	H-1→L+1(57%)	d(Ir)+π(C^N)→π*(C^N)	MLCT/LLCT/ILCT	
	S_{11}	296/4.17	0.166	H-3→L (72%)	d(Ir)+π(C^N+pic)→π*(C^N)	MLCT/LLCT/ILCT	
	S_{14}	287/4.31	0.254	H-3→L+1(60%)	d(Ir)+π(C^N+pic)→π*(C^N)	MLCT/LLCT/ILCT	
	T_1	461/2.68	0.000	H→L (54%)	d(Ir)+π(C^N)→π*(C^N)	MLCT/LLCT/ILCT	
3	S_1	502/2.46	0.211	H→L(97%)	d(Ir)+π(C^N)→π*(C^N)	MLCT/LLCT/ILCT	
	S_9	372/3.32	0.219	H-3→L+1(76%)	π(C^N)→π*(C^N)	LLCT/ILCT	
	S_{11}	359/3.44	0.182	H-4→L(98%)	π(C^N)→π*(C^N)	LLCT/ILCT	
	S_{48}	268/4.60	0.193	H-7→L+1(57%)	π(C^N+pic)→π*(C^N)	LLCT/ILCT	
	T_1	595/2.08	0.000	H→L (69%)	d(Ir)+π(C^N)→π*(C^N)	MLCT/LLCT/ILCT	
4	S_1	486/2.55	0.199	H→L(97%)	d(Ir)+π(C^N)→π*(C^N)	MLCT/LLCT/ILCT	
	S_2	466/2.66	0.118	H→L+1(96%)	d(Ir)+π(C^N)→π*(C^N)	MLCT/LLCT/ILCT	
	S_{11}	351/3.53	0.501	H-3→L+1(87%)	π(C^N)→π*(C^N)	LLCT/ILCT	
	S_{14}	339/3.64	0.186	H-5→L(59%)	π(C^N+pic)→π*(C^N)	LLCT/ILCT	
	S_{41}	272/4.54	0.188	H-3→L+5(50%)	π(C^N)→π*(C^N)	LLCT/ILCT	
	T_1	572/2.16	0.000	H→L (65%)	d(Ir)+π(C^N)→π*(C^N)	MLCT/LLCT/ILCT	

[a] Ref. 12

The experimental absorption spectrum for **1** show intense transitions at high energy

(below 270 nm) and weaker bands in the visible region (310-370 nm) with the tail extending into the visible region. For **1**, the strongest absorption with its oscillator strength of about 0.184 is calculated at 273 nm, which is very close to the experimental value 256 nm,[12] and the HOMO-5→LUMO configuration contributes 79% to this absorption. From the analysis on FMOs, it is reasonable to assign the absorptions to [d(Ir)+π(C^N)→π*(pic)] with metal to ligand charge transfer (MLCT) and intraligand charge transfer (ILCT) characters. Following the strongest absorption, there is a shoulder located at about 287 nm, which is mainly assigned to the HOMO-3→LUMO+1 (77%) transition and the corresponding oscillator strength is 0.154 with [π(C^N)→π*(C^N)]/LLCT/ILCT (intraligand charge transfer) character. Table 2 shows that the lowest-lying absorption bands for **1**–**4** are at 355, 370, 502 and 486 nm, respectively. This indicates that the lowest-lying absorptions for **2**–**4** are red-shifted (by 15, 147 and 131 nm respectively) compared with that of **1**, which is consistent with the trend of the HOMO-LUMO energy gaps because of the HOMO→LUMO transition with more than 90% in composition. The lowest energy absorptions of **1** is assigned as MLCT/LLCT transition characters and described as [d(Ir)+π(C^N)→π*(pic)] transitions. For **2**–**4**, the lowest absorption is ascribed to [d(Ir)+π(C^N)→π*(C^N)] with MLCT /LLCT /ILCT character, and their maximum absorption bands are located at 287, 372, 351 nm with the d(Ir)+π(C^N+pic)→π*(C^N) (for **2**) and [π(C^N)→ π*(C^N)] (for **3** and **4**) character.

For a better analysis of the excited state's nature, the natural transition orbital (NTO) based on TDDFT/PBE0 has been analyzed to assist the assignment of the electronic transition.[33,34] The occupied NTO can be seen as the “hole” orbital (i.e., the orbital from which electron is removed during transition), whereas “virtual” NTO is the orbital in which electron is placed in the excited state. The plots of the occupied and virtual NTOs correspond to electronic transitions from the ground state to the singlet excited states S1 and are shown in Fig. S1.

Phosphorescence properties

To check the computational method, four DFT functionals (M06HF, M062X, M052X

and B3LYP) were examined here (Table 3).

Table 3 Calculated phosphorescent emission wavelength (λ, in nm) for **1** in CH_2Cl_2 media with the TDDFT method at M06HF, M062X, M052X and B3LYP levels, respectively, together with the experimental value

	Exptl[a]	M06HF	M062X	M052X	B3LYP
1	462	464	504	532	572

[a] Ref. 12

For **1**, the calculated values with M052X and B3LYP functionals level deviate from experimental values by 70 and 110 nm, respectively. A good agreement with experimental data was obtained for M06HF, while a disagreement was found for M062X. Thus, the phosphorescence properties of complexes **1**–**4** were calculated at TD-DFT/M06HF level of theory in CH_2Cl_2 media on the basis of the optimized lowest triplet excited-state geometries.

The calculated emission energies, transition nature and the available experimental value are listed in Table 4.

Table 4 Phosphorescent emissions of **1**–**4** in CH_2Cl_2 medium at the TDDFT/M06HF level, along with experimental wavelength (nm)

	λ(nm)/E(eV)	Configuration	Nature	Exptl.[a]
1	464/2.66	L→H(89%)	^{3}MLCT/^{3}ILCT	462
2	485/2.55	L→H(85%)	^{3}MLCT/^{3}ILCT	
3	526/2.35	L→H(69%)	^{3}MLCT//^{3}ILCT	
4	505/2.45	L→H(69%)	^{3}MLCT/^{3}ILCT	

[a] Ref. 12

To conveniently discuss the transition property of emission, the calculated compositions of FMO related to emission for complexes **1**–**4** are listed in Table S5.

The calculated lowest-energy emission wavelength 464 nm for **1** is very close to the experimental data 462 nm. As revealed in Table S5, the HOMOs of the complexes have 40–60 % C^N and 30–40 % metal compositions, while the LUMOs of the complexes were mainly localized on C^N ligands. Therefore, the transitions of all complexes were assigned as ^{3}MLCT mixed with ^{3}LLCT and ^{3}ILCT. With respect to **1**, the excitation of [π*(C^N)→d(Ir)+π(C^N)] with the configuration coefficient of 0.89 causes the emission at 464 nm. Table S5 shows that HOMO-2 of the complexes are mainly consisted of Ir atom, while LUMO+12 of complexes **1** and **2**, and LUMO+18 of complexes **3** and **4** are localized on Ir atom. The energy gaps (ΔE) of d-d state are about 6.5 eV, which are obviously larger than HOMO-LUMO energy gaps (about 2.5 eV). In addition, it is also been found the HOMO-LUMO energy gap in complex **2** is smaller than that in complex **1**, while the energy gap of complex **3** is smallest. This indicated that when the electron-withdrawing ligand is localized at R1-position of phenyl in C^N ligands (Fig. 1 (a)), the HOMO-LUMO energy gap will decrease. Thus, it can be suspected that the introduction of the -F or -CN may make the emission band red shift.

Photoluminescence quantum efficiency

The quantum yield Φ_{PL} from an emissive excited state to the ground state is linked to the radiative (k_r) and the nonradiative (k_{nr}) rate constants by the following equation:

$$\Phi_{pL} = \frac{k_r}{k_r + k_{nr}} \quad (1)$$

Based on the Φ_{PL} and lifetime (τ_{em}) data for **1**,[12] calculated by applying the relations $k_r = \Phi_{PL}/\tau_{em}$ and $k_{nr} = (1-\Phi_{PL})/\tau_{em}$. The photophysical parameters for all complexes are summarized in Table 5. Theoretically, taking into account the lowest excited singlet and triplet states, k_r is inversely proportional to the energy difference ($\Delta E_{S_1\text{-}T_1}$) between the S_1 and T_1 states. The radioactive rate can be expressed by the following:[35,36]

$$k_r \approx \gamma \frac{\left\langle \Psi_{S_1} \left| H_{S_O} \right| \Psi_{T_1} \right\rangle^2 \mu_{S_1}^2}{(\Delta E_{S_1\text{-}T_1})^2}, \quad \gamma = \frac{16\pi^3 10^6 n^3 E_{T_1}^3}{3h\varepsilon_0} \qquad (2)$$

Herein, μ_{S_1} is the transition electric dipole moment in $S_0 \rightarrow S_1$ transition, E_{T_1} represents the emission energy in cm^{-1}, while n, h and ε_0 are the refractive index, Planck's constant and the permittivity in vacuum, respectively. The equation 2 shows that k_r increases with the increase of $\boldsymbol{E}_{\mathbf{T_1}}$. Thus, a large $\boldsymbol{E}_{\mathbf{T_1}}$ is essential for an efficient material. Table 5 indicates that **1** has the largest $\boldsymbol{E}_{\mathbf{T_1}}$ followed by **2**. Thus, the complexes **1** and **2** are a good candidate to be an efficient phosphorescent material.

Table 5 The contribution of ^{3}MLCT (%) in the T_1 state and the energy gaps between the S_1 and T_1 states ($\Delta E_{S_1\text{-}T_1}$) (in eV), along with the transition electric dipole moment in the $S_0 \rightarrow S_1$ transition μ_{S_1} (Debye) for the studied complex **1** in CH_2Cl_2 medium

	^{3}MLCT	$\Delta E_{S_1\text{-}T_1}$	$\boldsymbol{E}_{\mathbf{T_1}}$	μ_{S_1}
1	38.27	0.5019	2.66	0.27
2	36.55	0.4561	2.55	2.95
3	28.98	0.8104	2.35	1.95
4	31.74	0.8761	2.45	2.98

The photophysical properties of organometallic triplet emitters depend on the metal participation in the triplet states and on the effective spin-orbit coupling (SOC). The SOC effects are elucidated mainly from the following two aspects. One is the contribution of ^{3}MLCT in the T_1 state.[37] As presented by Chou et al.,[38] the ^{3}MLCT can be calculated as follows:

CT(M) = %(M)HOMO-x - %(M)LUMO+y

where %(M)HOMO-x and %(M)LUMO+y are electronic densities on the metal in HOMO-x and LUMO+y. The direct involvement of the Ir(d) orbital can enhances the first-order SOC in the $T_1 \rightarrow S_0$ transition, which would result in a drastic decrease of the radiative lifetime and avoid the nonradiative process.[39] A large ^{3}MLCT contribution is beneficial to increase the quantum yield (Φ_{PL}). Table 6 shows that the contribution of ^{3}MLCT is calculated to be 38.27 %, 36.55 %, 28.98 %, and 31.74 % for **1**–**4**, respectively. The highest ^{3}MLCT is found in **1** and **2**, indicating a chance for high Φ_{PL}. On the other hand, strong SOC and fast ISC rate between the S_1 and T_1 excited states requires these two states to be close in the energy gaps between the S_1 and T_1 states ($\Delta E_{S_1\text{-}T_1}$), leading to the increased k_r. The $\Delta E_{S_1\text{-}T_1}$ decreases with the order of **4** > **3** > **1** > **2**. Among them, the **2** has the smallest $\Delta E_{S_1\text{-}T_1}$. From the above discussion, it can be concluded that complex **2** with stronger SOC, better ISC rate, and faster radiative decay leads to its higher photoluminescent quantum efficiency than others studied in this paper. From the equation 2, we can see that a larger μ_{S_1} will lead to an increase of k_r. As for μ_{S_1}, the largest values calculated were 2.95 D and 2.98 D for **2** and **4**, respectively, implying their higher k_r values. Through the above analysis, the complex **2** with a relatively larger k_r could be the potential blue phosphorescence emitters for OLED with high quantum efficiency.

Comparison of performance in OLEDs

The charge injection properties of luminescent materials can be evaluated by the electron affinity (EA) and ionization potential (IP), which are also closely related to the LUMO and HOMO, respectively. A smaller IP value means easier hole injection ability, whereas larger EA value will facilitate electron injection. In this section, IP, EA, and reorganization energy (λ) are calculated, together with hole extraction potential (HEP) and electron extraction potential (EEP).

To confirm the estimate's validity, the calculated vertical IP (IP_v), adiabatic IP (IP_a), vertical EA (EA_v), and adiabatic EA (EA_a), together with hole extraction

potential (HEP) and electron extraction potential (EEP), are listed in Table 6. The IP_v is defined as the energy difference between the cation and its neutral molecule at the equilibrium geometry of the neutral molecule. The IP_a is defined as the energy difference between the cation and its neutral molecule at their own equilibrium geometries. The EA_v is defined as the energy difference between the neutral molecule and its anion both at the equilibrium geometry of the anion. The EA_a is defined as the energy difference between the neutral molecule and its anion at their own equilibrium geometries.[40]

Table 6 Ionization potentials (IP_v and IP_a), electronic affinities (EA_v and EA_a), hole extraction potential (HEP), electron extraction potential (EEP) and reorganization energies for hole/ electron transfer (λ_h and λ_e) of **1**–**4** (in eV)

	IP_v	IP_a	EA_v	EA_a	HEP	EEP	λ_h	λ_e
1	6.58	6.48	0.39	0.49	6.36	0.62	0.27	0.21
2	6.69	6.58	0.90	1.03	6.46	1.03	0.18	0.12
3	7.18	7.04	2.55	2.65	6.82	2.78	0.24	0.22
4	7.50	7.35	2.87	2.98	7.08	3.10	0.42	0.23

The results show that **2** have smaller IP value and larger hole injection abilities compared with **3** and **4**, which is consistent with its higher HOMO energy level (Fig. 2). The experimentally obtained complex **1** has the smallest IP value, which is consistent with its highest HOMO energy level. This means that the hole injection is much easier in complex **1** than others. The calculated EA (both vertical and adiabatic) values increase in the following order: **1** < **2** < **3** < **4**. Corresponding to the lowest LUMO energy level, the assumed complex **4** has large EA value and enhanced electron injection ability as compared to the complexes **1**–**3**.

According to semiclassical Marcus/Hush model,[41] the charge (hole or electron) transfer rate *k* can be expressed by the following formula:

$$\kappa = \mathrm{A}\exp\left(-\frac{\lambda}{4\kappa_b T}\right) \quad (3)$$

where A is a prefactor related to the electronic coupling between adjacent molecules, λ is the reorganization energy, and κ_b is the Boltzmann constant, T is the temperature. Therefore, the mobility of charges has been demonstrated to be dominantly related to the reorganization energy (λ) for OLEDs materials and the low λ value is necessary for an efficient charge transport process. The reorganization energy for hole/electron transfer can be simply defined as follows: $\lambda_h = IP_v - HEP$ and $\lambda_e = EEP - EA_v$. As emitting-layer materials, they need to achieve balance between hole injection and electron acceptance. Furthermore, the lower the λ value is, the higher the charge transport rate is. Herein, one can find that complex **2** has the best hole transfer ability with the smallest λ_h value (Table 6). The nearly identical λ_e values of **1**, **3** and **4** indicate that they may have comparable electron transfer abilities. The reorganization energies indicate that the differences between λ_h and λ_e for **1**–**3** (0.06, 0.06 and 0.02 eV, respectively) are small, especially for **3**. So hole and electron transfer balance could be achieved easily in emitting layer, which is the key factor for materials used in OLEDs.

Conclusions

This theoretical work reported the investigation of geometrical structures, absorptions, injection, and transport abilities, phosphorescence mechanism of four iridium(III) cyclometalated complexes with the 2,5-Diaryl-1,3,4-oxadia-zoles (OXDs) moiety in C^N ligands. Based on the detailed discussion above, the following conclusions can be drawn:

(1) The calculated results reveal that the introduction of the cyano functional group in the phenyl-ring of C^N ligands in complexes **3** and **4** have the lower HOMO and LUMO energies than those of **1** and **2**, which will consequently results in the easier electron injections into **3** and **4**, and the easier hole injections into **1** and **2**.

(2) The electron densities of the frontier molecular orbital distributions are also influenced by different substitution on C^N ligands of these complexes. However, absorption spectra for **1** and **2** show the similar pattern in the absorption curves. The

lowest-lying singlet absorptions of **2**–**4** are significantly red-shifted compared with that of the parent complex **1**, indicating that the variation of substitution in C^N ligand causes remarkable influence on the absorption spectra.

(3) The emission color can be affected by changing π electron-withdrawing ability of the C^N ligands, which is very practical to explore the relationship between the substituent and the phosphorescence of the Ir(III) complexes. The designed complex **2** is potential candidate for blue phosphorescent material.

Acknowledgements

The authors thank the Science and Technology Research Project for the Twelfth Five-year Plan of Education Department of Jilin Province of China (Grant No. 2015110) and the Project Funded by China Postdoctoral Science Foundation (Grant No. 2015M571337).

References

1 M. Mazzeo, V. Vitale, F. Della Sala, M. Anni, G. Barbarella, L. Favaretto, G. Sotgiu, R. Cingolani and G. Gigli, *Adv. Mater*., 2005, **17**, 34–39.

2 A. Tsuboyama, H. Iwawaki, M. Furugori, T. Mukaide, J. Kamatani, S. Igawa, T. Moriyama, S. Miura, T. Takiguchi, S. Okada, M. Hoshino and K. Ueno, *J. Am. Chem. Soc*., 2003, **125**,12971–12979.

3 D. M. Han, Y. H. Wu, H. X. Cai, C. Y. Pang and L. H. Zhao, *Snythetic Met.*, 2015, **209**, 455–460.

4 M. A. Baldo, D. F. O' Brien, Y. You, A. Shoustikov, S. Sibley, M. E. Thompson and S. R. Forrest, *Nature* 1998, **395**, 151–154.

5 S. Lamansky, P. Djurovich, D. Murphy, F. Abdel-Razzaq, H. E. Lee, C. Adachi, P. E. Burrows, S. R. Forrest and M. E. Thompson, *J. Am. Chem. Soc*., 2001, **123**, 4304–4312.

6 M. L. Ho, F. M. Hwang, P. N. Chen, Y. H. Hu, Y. M. Cheng, K. S. Chen, G. H. Lee, Y. Chi and P. T. Chou, *Org. Biomol. Chem*., 2006, **4**, 98–103.

7 M. Schmittel and H. W. Lin, *Inorg. Chem*., 2007, **46**, 9139–9145.

8 K. Koike, N. Okoshi, H. Hori, K. Takeuchi, O. Ishitani, H. Tsubaki, I. P. Clark, M. W. George, F. P. A. Johnson and J. J. Turner, *J. Am. Chem. Soc*., 2002, **124**, 11448–11455.

9 S. Zalis, I. R. Farrell and A. Vlcek, *J. Am. Chem. Soc*., 2003, **125**, 4580–4592.

10 A. P. Kulkarni, C. J. Tonzola, A. Babel and S. A. Jenekhe, *Chem. Mater*., 2004, **16**, 4556–4573.

11 G. Hughes and M. R. Bryce, *J. Mater. Chem*., 2005, **15**, 94–107.

12 Y. Zheng, A. S. Batsanov and M. R. Bryce, *Inorg. Chem*., 2011, **50**, 3354−3362.

13 J. P. Perdew, K. Burke and M. Ernzerhof, *Phys. Rev. Lett*., 1997, **78 (7)**: 1396−1396.

14 C. Adamo and V. Barone, *J. Chem. Phys*., 1999, **110**, 6158−6170.

15 T. Liu, B. H. Xia, Q. C. Zheng, X. Zhou, Q. J. Pan and H. X. Zhang, *J. Comput. Chem*., 2010, **31**, 628−638.

16 I. Ciofini, P. P. Laine, F. Bedioui and C. Adamo, *J. Am. Chem. Soc*., 2004, **126**, 10763−10777.

17 J. Autschbach, T. Ziegler, S. J. A. Gisbergen and E. J. Baerends, *J. Chem. Phys*., 2002, **116**, 6930−6940.

18 T. Helgaker and P. Jørgemsen, *J. Chem. Phys*., 1991, **95**, 2595−2601.

19 K. L. Bak, P. Jørgemsen, T. Hel-gaker, K. Rund and H. J. A. Jensen, *J. Chem. Phys*., 1993, **98**, 8873−8887.

20 E. Cancès, B. Mennucci and J. Tomasi, *J. Chem. Phys*., 1997, **107**, 3032−3041.

21 M. Cossi, V. Barone, B. Mennucci and J. Tomasi, *Chem. Phys. Lett*., 1998, **286**, 253−260.

22 B. Mennucci and J. Tomasi, *J. Chem. Phys*., 1997, **106**, 5151−5158.

23 Y. Zhao and D. G. Truhlar, *J. Phys. Chem. A*, 2006, **110**, 13126−13130.

24 Y. Zhao and D. G. Truhlar, *Theor. Chem. Acc*., 2008, **120**, 215−241.

25 Y. Zhao, N.E. Schultz and D.G. Truhlar, *J. Chem. Theory Comput*., 2006, **2**, 364.

26 A.D. Becke, *J. Chem. Phys*. 1993, **98**, 5648−5652.

27 P. J. Hay and W. R. Wadt, *J. Chem. Phys*., 1985, **82**, 270–283.

28 P. C. Hariharan and J. A. Pople, *Mol. Phys*., 1974, **27**, 209–214.

29 M. J. Frisch, G. W. Trucks, H. B. Schlegel, G. E. Scuseria, M. A. Robb, J. R. Cheeseman, G. Scalmani, V. Barone, B. Mennucci, G. A. Petersson, H. Nakatsuji, M. Caricato, X. Li, H. P. Hratchian, A. F. Izmaylov, J. Bloino, G. Zheng, J. L. Sonnenberg, M. Hada, M. Ehara, K. Toyota, R. Fukuda, J. Hasegawa, M. Ishida, T. Nakajima, Y. Honda, O. Kitao, H. Nakai, T. Vreven, J. A. Montgomery Jr, J. E. Peralta, F. Ogliaro, M. Bearpark, J. J. Heyd, E. Brothers, K. N. Kudin, V. N. Staroverov, T. Keith, R. Kobayashi, J. Normand, K. Raghavachari, A. Rendell, J. C. Burant, S. S. Iyengar, J. Tomasi, M. Cossi, N. Rega, J. M. Millam, M. Klene, J. E. Knox, J. B. Cross, V. Bakken, C. Adamo, J. Jaramillo, R. Gomperts, R. E. Stratmann, O. Yazyev, A. J. Austin, R. Cammi, C. Pomelli, J. W. Ochterski, R. L. Martin, K. Morokuma, V. G. Zakrzewski, G. A. Voth, P. Salvador, J. J. Dannenberg, S. Dapprich, A. D. Daniels, O. Farkas, J. B. Foresman, J. V. Ortiz, J. Cioslowski and D. J. Fox, *Gaussian 09* (*Revision B.01*), Gaussian, Inc., Wallingford, CT, 2010.

30 N. M. O'Boyle, A. L. Tenderholt and K. M. Langner, *J. Comput. Chem*., 2008, **29**, 839–845.

31 J. Zhou, J. L. Sonnenberg and H. B. Schlegel, *Inorg. Chem*., 2010, **49**, 6545–6551.

32 Q. Cao, J. Wang, Z. S. Tian, Z. F. Xie and F. Q. Bai, *J. Comput. Chem*., 2012, **33**, 1038−1046.

33 R. L. Martin, *J. Chem. Phys.*, 2003, **118**, 4775−4777.

34 J. D. Chai, M. Head-Gordon, *Phys. Chem. Chem. Phys.*, 2008, **10**, 6615−6620.

35 S. Haneder, E. Da Como, J. Feldmann, J. M. Lupton, C. Lennartz, P. Erk, E. Fuchs, O. Molt, I. Munster, C. Schildknecht and G. Wagenblast, *Adv. Mater*., 2008, **20**, 3325–3330.

36 N. Turro, *Modern Molecular Photochemistry*, University Science Books, Palo Alto, USA, 1991.

37 J. Li, P. I. Djurovich, B. D. Alleyne, M. Yousufuddin, N. N. Ho, J. C. Thomas, J. C. Peters, R. Bau and M. E. Thompson, *Inorg. Chem*., 2005, **44**, 1713−1727.

38 Y. M. Cheng, E. Y. Li, G. H. Lee, P. T. Chou, *Inorg. Chem.*, 2007, **46**, 10276−10286.

39 I. Avilov, P. Minoofar, J. Cornil and L. De Cola, *J. Am. Chem. Soc*., 2007, **129**, 8247−8258.

40 J. C. Rienstra-Kiracofe, G. S. Tschumper, H. F. Schaefer, S. Nandi, G. B. Ellison, *Chem. Rev.*, 2002, **102**, 231−282.

41 N. S. Hush, *J. Chem. Phys*., 1958, **28**, 962−972.